RESEARCH ARTICLE | OCTOBER 08 2024

Propensity of hydroxide and hydronium ions for the air–water and graphene–water interfaces from *ab initio* and force field simulations

Laura Scalfi ; Louis Lehmann ; Alexandre P. dos Santos ; Maximilian R. Becker ; Roland R. Netz

J. Chem. Phys. 161, 144701 (2024)
https://doi.org/10.1063/5.0226966

The Journal of Chemical Physics ARTICLE pubs.aip.org/aip/jcp

Propensity of hydroxide and hydronium ions for the air–water and graphene–water interfaces from *ab initio* and force field simulations

Cite as: J. Chem. Phys. 161, 144701 (2024); doi: 10.1063/5.0226966
Submitted: 5 July 2024 • Accepted: 19 September 2024 •
Published Online: 8 October 2024

Laura Scalfi,[1] Louis Lehmann,[1] Alexandre P. dos Santos,[2] Maximilian R. Becker,[1] and Roland R. Netz[1,a)]

AFFILIATIONS

[1] Fachbereich Physik, Freie Universität Berlin, Arnimallee 14, 14195 Berlin, Germany
[2] Instituto de Física, Universidade Federal do Rio Grande do Sul, Caixa Postal 15051, CEP, 91501-970 Porto Alegre, RS, Brazil

[a)] **Author to whom correspondence should be addressed:** rnetz@physik.fu-berlin.de

ABSTRACT

Understanding acids and bases at interfaces is relevant for a range of applications from environmental chemistry to energy storage. We present combined *ab initio* and force-field molecular dynamics simulations of hydrochloric acid and sodium hydroxide highly concentrated electrolytes at the interface with air and graphene. In agreement with surface tension measurements at the air–water interface, we find that HCl presents an ionic surface excess, while NaOH displays an ionic surface depletion, for both interfaces. We further show that graphene becomes less hydrophilic as the water ions concentration increases, with a transition to being hydrophobic for highly basic solutions. For HCl, we observe that hydronium adsorbs to both interfaces and orients strongly toward the water phase, due to the hydrogen bonding behavior of hydronium ions, which donate three hydrogen bonds to bulk water molecules when adsorbed at the interface. For NaOH, we observe density peaks of strongly oriented hydroxide ions at the interface with air and graphene. To extrapolate our results from concentrated electrolytes to dilute solutions, we perform single ion-pair *ab initio* simulations, as well as develop force-field parameters for ions and graphene that reproduce the density profiles at high concentrations. We find the behavior of hydronium ions to be rather independent of concentration. For NaOH electrolytes, the force-field simulations of dilute NaOH solutions suggest no hydroxide adsorption but some adsorption at high concentrations. For both interfaces, we predict that the surface potential is positive for HCl and close to neutral for NaOH.

INTRODUCTION

The behavior of acids and bases at interfaces is of relevance for a range of applications, such as environmental and atmospheric chemistry,[1] prebiotic chemistry,[2] biological processes, heterogeneous catalysis, and energy storage.[3] In these systems, understanding the composition of the interface is of paramount importance, as it determines, for example, the reactivity of microdroplets,[4] the performances of energy storage devices such as supercapacitors,[5] or the local environment in which cellular membranes evolve. Electrostatic continuum theory predicts the repulsion of ions in an aqueous electrolyte from interfaces with a dielectric medium of lower dielectric constant, such as air.[6] However, several experimental and theoretical studies have shown that, even for simple monovalent ions at the air–water interface, this simple image charge picture is challenged: in particular, H_3O^+ ions are found to adsorb at the interface with air.[7–12] Several factors such as ion size, polarizability, solvation free energy, and interfacial curvature were found to play a role in the propensity of ions for the air–water interface.[13]

The air–water interface is commonly studied because it is simple, ubiquitous, and easily probed in experimental setups.[14] However, the influence of other materials is relevant for industrial applications and studies have focused on hydrophobic interfaces,[15–19] either using a homogeneous wall or a graphene sheet. Some studies have found remarkably similar potentials of mean force (PMF) for ions at the interface with air and with hydrophobic interfaces, leading to the concept of a generic hydrophobic effect. However, free energy decomposition into entropic and enthalpic effects shows

that the similar propensity of ions for these interfaces might come from a cancellation of different contributions,[17] such as interface pinning by ions, capillary-wave and interfacial-roughness effects, ion–graphene interactions or hydrogen bonding.

Among monovalent ions, the ions of the autoprotolysis of water, hydronium, and hydroxide have sparked particular debate, due to contradicting experimental and theoretical evidence.[20,21] On the one hand, surface tension measurements of the air–water interface at varying salt concentrations up to several mol/l show a depletion of ions for salts and bases but a positive ionic excess for acids,[22–25] indicating the adsorption of hydronium ions at the air–water interface. On the other hand, electrokinetic measurements of the ζ-potential of air bubbles, in a range of pH values from 2 to 12, show that, above a pH of 2–4, the air–water interface is negatively charged,[26–30] which has been interpreted as being caused by hydroxide adsorption,[28,29,31,32] charge transfer between water molecules,[33,34] or negatively charged impurities (organic molecules and surfactants) that accumulate at the interface.[35–38] None of these theories have, however, created a large consensus.[39–43]

Spectroscopic measurements also yield a variety of results regarding the electrolyte–air interfaces: second harmonic generation (SHG) and sum-frequency generation (SFG) spectroscopy show strong hydronium adsorption for highly acidic electrolytes,[44–46] while results for highly basic solutions report both hydroxide repulsion from the interface[47] and moderate adsorption.[45,48] Recent measurements, however, agree on the substantially stronger surface affinity of hydronium compared to hydroxide.[49,50]

Many theoretical studies addressed water ions at the air–water interface, which, however, also yielded contradictory results. Early density functional theory (DFT) studies found no affinity of hydronium for the air–water interface,[51,52] while most found hydronium adsorption,[7–9] in agreement with classical non-polarizable[7,11,12] and polarizable[53,54] force field (FF) studies. In addition, simulations using empirical valence bond (EVB) reactive force fields also found varying results.[15,55–58] In the case of hydroxide, the results are even more widespread: some DFT and FF molecular dynamics (MD) studies predicted hydroxide adsorption to the air–water interface,[59,60] while other showed a repulsion from it.[7,11] These methods suffer from several drawbacks, which could explain the diverging results: in the case of DFT, proper equilibration is challenging due to the short timescales accessible, and, to obtain a potential of mean force (PMF) from a single ion, enhanced sampling methods such as umbrella sampling are typically used, which interfere with the Grotthuss mechanism. This could impact the system's reorientation dynamics and worsen the sampling. In the case of non-reactive FF studies, autoprotolysis and Grotthuss mechanisms are also entirely suppressed and hydronium and hydroxide ions are treated as fixed entities, but the long simulation times allow for an accurate sampling of static properties. However, FF results depend drastically on the parameters of the force field, which are notoriously hard to develop for hydroxide ions. Recent neural network MD simulations, which ally the accuracy of DFT functionals with the sampling efficiency of classical MD simulations, found hydronium adsorption and hydroxide repulsion from the air–water interface.[50,61]

Here, we proceed differently and investigate highly concentrated electrolytes, relevant for many biological, environmental, and energy-device applications, using extensive unbiased DFT-MD simulations of HCl and NaOH. The large number of ions in the system allows us to collect enough statistics within the simulation times available using high performance computing. We concentrate on the molecular origin of the ionic propensities we observe, in terms of molecular orientation, local electrostatic potential, and hydrogen bonding. To study the dilute limit, we develop force fields using the high concentration DFT results as reference.

Because of the relevance of graphene and its derivatives in various applications,[62–66] in particular in membranes and nanofluidic devices, we study the graphene–water interface in addition to the air–water interface. Recent theoretical studies have investigated hydronium[67,68] in graphene nanochannels and hydroxide[19,69,70] at graphene–water interfaces. These show a large adsorption of hydroxide at the interface, which would agree with electrokinetic measurements that suggest a negative surface charge at the pristine graphene–water interface.[71–73] A large propensity of both hydronium and hydroxide for the graphene sheet was also found using a polarizable model.[74] These results for graphene can also be compared to studies on generic hydrophobic interfaces.[19] Note that graphene is not rigorously hydrophobic, as water on graphene has a contact angle of ~80°,[75] although the water layer in contact with graphene structurally resembles that at the air–water interface.

In the following, we discuss ionic density, orientation, and electric field profiles at these two interfaces, where both ions show strongly opposite orientations. We show that their interfacial behavior is due to the molecular nature of these ions and analyze in particular their hydrogen bonding. We show that HCl presents an ionic surface excess, while NaOH displays an ionic surface depletion at both interfaces, in agreement with surface tension measurements on air bubbles. We calculate the contact angle of these solutions on graphene and find that it becomes less hydrophilic for increasing concentration, with a transition to being hydrophobic for highly basic solutions. We also predict for both interfaces that the surface potential is positive for HCl and close to neutral for NaOH.

METHODS

In this work, we perform extensive density functional theory molecular dynamics simulations of hydrochloric acid (HCl) and sodium hydroxide (NaOH) solutions, at the interface with air and a graphene sheet. To avoid introducing biases on the coordination number for the hydroxide and hydronium ions that could have a non-trivial impact on the Grotthuss mechanism, we consider concentrated electrolytes (> 6 mol/l), for which the sampling is improved by the increased number of ions in solution. The setups for the HCl solutions contain a slab of 291 water molecules, 45 hydronium ions, and 45 chloride ions, corresponding to 6.5 and 6.7 mol/l at the interface with air and graphene, respectively. For the NaOH solutions, we consider 315 water molecules, 37 hydroxide ions, and 37 sodium ions, corresponding to 9.1 and 8.6 mol/l at the interface with air and graphene, respectively. For the systems at the interface with graphene, two graphene sheets of 160 carbon atoms each are placed on either side of the liquid slab (we leave a layer of vacuum on the other side of the graphene sheets). The box sizes are fixed at 21.3 × 19.7 Å^2 in the xy plane and L_z = 60 Å in the z-direction, normal to the interface. Periodic boundary conditions (PBCs) are used in all directions. The final simulation boxes are shown in Figs. 1(a), 1(b), 2(a), and 2(b). After equilibration, the

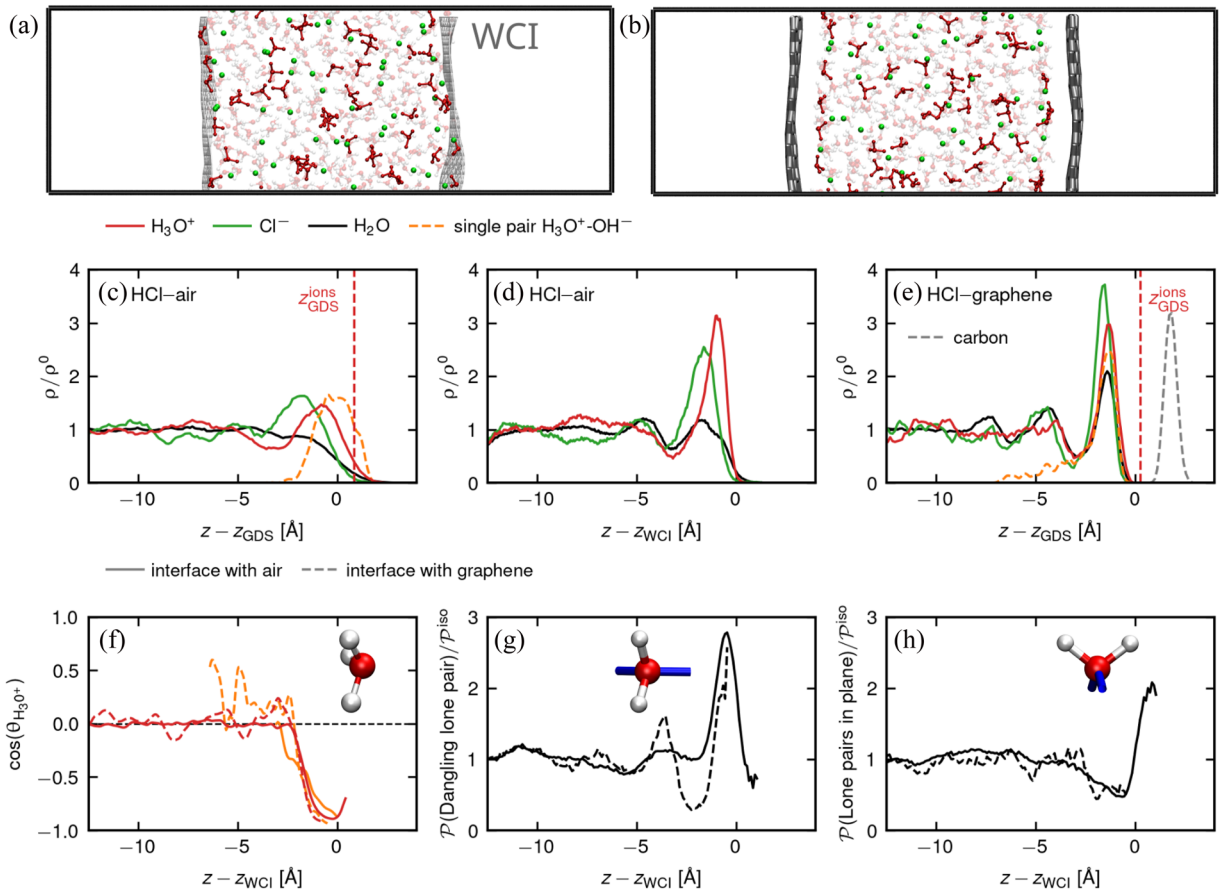

FIG. 1. Hydronium at interfaces. (a) and (b) Snapshots of the simulation boxes for the HCl–air (a) and HCl–graphene systems (b). The water molecules are shown as transparent, the chloride ions are shown in green, the hydronium ions are shown in dark red, and the carbon atoms are shown in gray. In panel (a), we also show the Willard–Chandler interface (WCI) in light gray. (c)–(e) Density profiles ρ of hydronium ions (red lines), chloride ions (green lines), water (black lines), and carbon (gray dashed line) as a function of the distance to the GDS [(c) and (e)] or to the WCI (d), for an air–water interface [(c) and (d)] and for a graphene–water interface (e), normalized by the bulk density ρ^0. The orange dashed lines are hydronium profiles for the single ion pair H_3O^+–OH^- system. (f) Average orientation of the hydronium ion dipole moment as a function of the distance to the WCI, for the air–water interface (solid lines) and for the graphene–water interface (dashed lines), for the concentrated electrolyte (red lines) and for the single ion pair H_3O^+–OH^- (orange lines). (g) and (h) Probability profile as a function of the distance to the WCI, for the interface with air (solid lines) and graphene (dashed lines), of finding a given water molecule orientation, normalized by the isotropic bulk probability. Data are shown for the dangling lone pair orientation (g) and for the orientation with two lone pairs in a plane parallel to the surface (h). The sketches show these orientations, using blue sticks to visualize the two lone pairs of the water oxygen atom.

aqueous slabs between the two interfaces with air have a thickness of about 26 Å for HCl and 22 Å for NaOH, while for the systems with graphene surfaces, the distance between the two graphene sheets is 30 Å for HCl and 26 Å for NaOH. We also compare our results with previously published DFT-MD simulations of a pure air–water interface[43] and a pure graphene–water interface.[76] The system sizes are similar to the current setup: in the air–water system, the water slab has a thickness of 24 Å, while in the graphene–water system, the distance between the graphene sheets is 34 Å. We note that in these pure water simulations, the graphene sheets are kept rigid and immobile, while they are allowed to be flexible and to translate in our setup.

All systems are created and pre-equilibrated using the GROMACS software[77] and the non-polarizable force field (FF) developed by Bonthuis *et al.*[78] The DFT-MD equilibration and production runs are performed with the software CP2K,[79] using the BLYP functional[80,81] with Grimme D3 dispersion correction[82] with a cutoff of 600 Ry. We use the DZVP-MOLOPT-SR basis set[83] for all atoms except for Cl^-, combined with Goedecker–Teter–Hutter (GTH) pseudo-potentials.[84] For the anion Cl^-, we use the aug-DZVP basis set that includes more diffuse functions,[85] as done previously.[86]

The DFT-MD simulations are run within the Born–Oppenheimer approximation with a canonical sampling through velocity rescaling (CSVR) thermostat at 300 K, with a time step of 0.5 fs. Starting from a FF-MD equilibrated configuration, the systems are re-equilibrated using DFT-MD for 10 ps, and then, a production run is performed for at least 75 ps for the interfaces with graphene and 140 ps for the interfaces with air. For the HCl–air systems, we ran in parallel three uncorrelated simulations for better statistics.

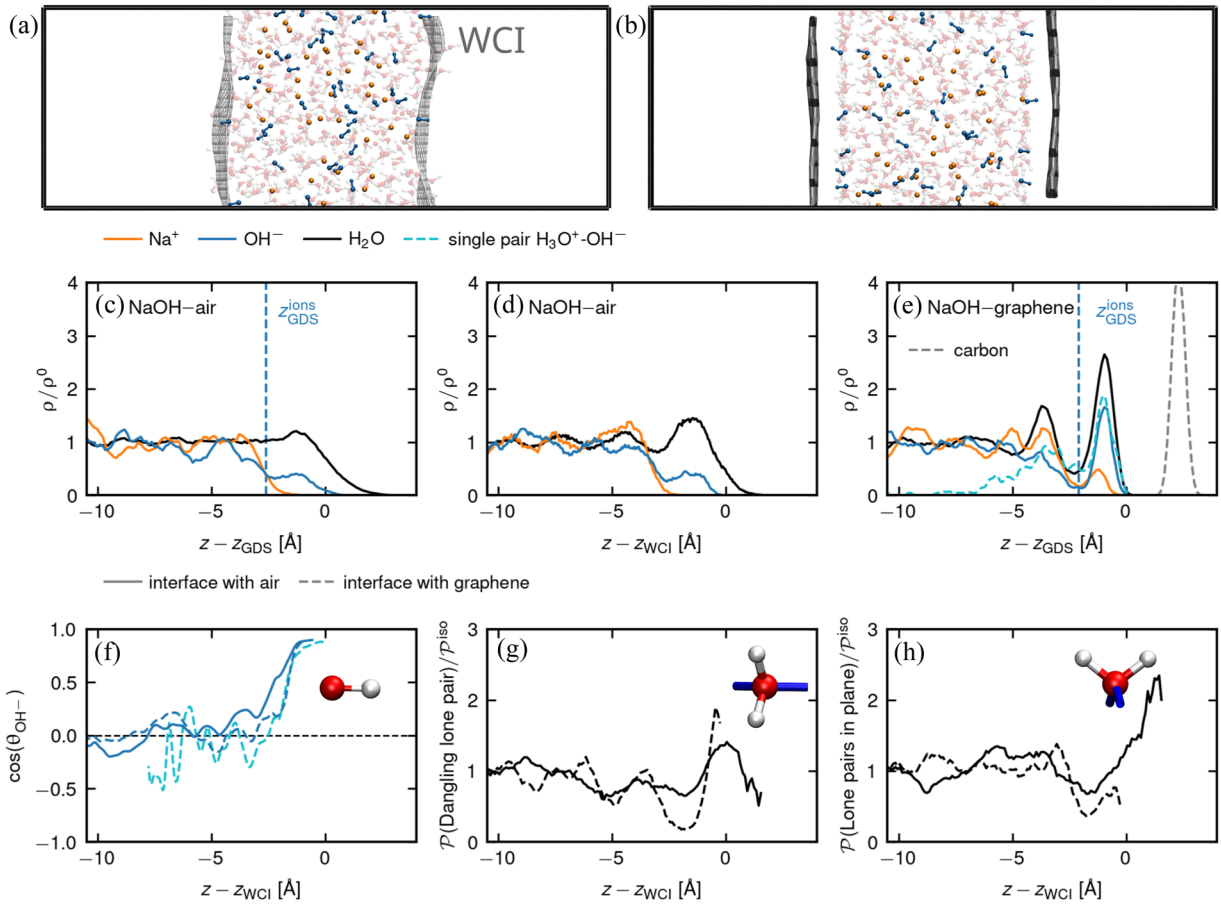

FIG. 2. Hydroxide at interfaces. (a) and (b) Snapshots of the simulation boxes for the NaOH–air (a) and the NaOH–graphene systems (b). The water molecules are shown as transparent, the sodium ions are shown in orange, the hydroxide ions are shown in blue, and the carbon atoms are shown in gray. In panel (a), we also show the Willard–Chandler interface (WCI) in light gray. (c)–(e) Density profiles ρ of hydroxide ions (blue lines), sodium ions (orange lines), water (black lines), and carbon (gray dashed line) as a function of the distance to the GDS [(c) and (e)] or to the Willard–Chandler interface (d), for the air–water interface [(c) and (d)] and for the graphene–water interface (e), normalized by the bulk density ρ^0. The cyan dashed lines are hydroxide profiles for the single ion pair H_3O^+–OH^- system. Note that the results for the hydroxide ion in the single ion pair setup at the air–water interface are not shown since the single ion was initially placed in the bulk to ensure electroneutrality and does not sample the interface during the simulation. (f) Average orientation of the hydroxide ion dipole moment as a function of the distance to the WCI, for the air–water interface (solid lines) and for the graphene–water interface (dashed lines), for the concentrated electrolyte (blue lines) and for the single ion pair H_3O^+–OH^- (cyan lines). (g) and (h) Probability profile as a function of the distance to the WCI, for the interface with air (solid lines) and with graphene (dashed lines), of finding a given water molecule orientation, normalized by the isotropic bulk probability. Data are shown for the dangling lone pair orientation (g) and for the orientation with two lone pairs in a plane parallel to the surface (h). The sketches show these orientations, using blue sticks to visualize the two lone pairs of the water oxygen atom.

To check that the high concentrations used in this work do not have a qualitative impact on the ion–interface interactions and to compare with earlier studies, in particular the work from Grosjean *et al.*[70] on hydroxide at the graphene–water interface, we run additional DFT-MD simulations of a water slab in contact with air or in contact with a graphene sheet, in which we introduce single ion pairs directly at the interface to observe their dynamics. In the simulations of Ref. 70, the simulation box was not charge-neutral, which might have an impact on the free energy profiles at interfaces;[87] instead, we place a hydroxide ion as well as a hydronium counter ion in the simulation box. For the air–water interface, we place the hydronium ion at the interface, while the hydroxide ion is in the bulk. For the graphene–water interface, both the hydroxide and hydronium ions are placed on the graphene sheet, each on one side, as far away as possible from each other in the *xy* plane. The cumulative length of single ion-pair simulations is 26 ps for the air–water interface and 80 ps for the graphene–water interface. More details on the specific setups, as well as snapshots of the systems and single-ion trajectories, are given in Sec. S1 of the supplementary material. Due to the relatively short simulation length with respect to the timescale for one ion to diffuse through the whole water slab, the density profiles shown are highly dependent on the initial condition but allow us to estimate the local potential of mean force and orientation preference. To be able to compare our results with Ref. 70, we use, for

these single ion pair simulations only, the PBE-D3 functional[80,88,89] at 323.15 K. All other parameters are the same as detailed above.

In the DFT simulations, the hydroxide and hydronium ions are not fixed entities as protons are transferred to or from neighboring water molecules. In our analysis, we therefore attribute each proton to the nearest oxygen atom and then count the number of hydrogen atoms per oxygen to distinguish water molecules from hydronium or hydroxide ions.

INTERFACE PROPENSITY OF HYDRONIUM H_3O^+

We first investigate the propensity of ions for hydrophobic interfaces in the case of the concentrated HCl electrolyte by computing density profiles in the z-direction, normal to the interface, as shown in Figs. 1(c)–1(e). The ionic and water profiles are normalized by the ionic and water bulk densities, respectively, and symmetrized with respect to the center of mass of the slab. To compare the different systems, we use the Gibbs Dividing Surface (GDS) defined as

$$z^{\mathrm{X}}_{\mathrm{GDS}} = \frac{L_z}{2} + \int_{L_z/2}^{L_z} \frac{\rho_{\mathrm{X}}(z)}{\rho^0_{\mathrm{X}}}\,\mathrm{d}z, \tag{1}$$

where ρ_{X} is the number density profile of species X, with X $\in$ {ions, water, solution}, and ρ^0_{X} is its bulk value. The bulk densities are determined by averaging the ionic or water densities in the middle of the liquid slab. The integration goes from the middle of the slab $L_z/2$ into the vacuum (where the density is zero). The GDS corresponds to the length of the effective box model of density ρ^0_{X} that contains the same number of molecules in the slab (because of symmetry, the box model length is $2z^{\mathrm{X}}_{\mathrm{GDS}}$ in our case). Note that, due to electroneutrality, the ionic GDS is the same for cations and anions and denoted as $z^{\mathrm{ions}}_{\mathrm{GDS}}$. In Figs. 1(c) and 1(e), the profiles are plotted with respect to the GDS of the solution, including both water and ions. In the following, we will denote the solution GDS simply as GDS and indicate its position by z_{GDS}. Alternatively in Fig. 1(d), we consider profiles with respect to the Willard–Chandler interface[90] (WCI), as used previously.[8,58] This construction results in an instantaneous and locally flexible interface, which allows us to suppress the broadening of the profiles due to interface roughening.[91] This is mostly relevant for the air–water interfaces, but we use it for graphene–water interfaces in some cases, to keep consistency. Details on the construction of the WCI are given in Sec. S2 of the supplementary material.

The number density profiles of HCl at the interface with air with respect to the GDS in Fig. 1(c) show a sigmoidal shape for water and a clear accumulation of hydronium ions as well as chloride ions at the interface, similar to the results obtained from FF-MD simulations.[11] The same profiles as a function of the distance to the WCI, shown in Fig. 1(d), reveal a two-layer hydration structure of water at the interface. Note that we only have a single clear hydration peak for the pure air–water interface (see Fig. S3 of the supplementary material). The hydronium and chloride density peaks at the interface coincide with the first hydration layer; they are narrower and higher when plotted as a function of the distance to the WCI [see Fig. 1(d)] compared to the profiles in Fig. 1(c), with a local accumulation up to three times their bulk density. Importantly, the ions form a double-layer at the interface, with the hydronium peak closer to the air than the chloride one. At the interface with graphene, shown in Fig. 1(e), we observe three density peaks for the water, at least one for hydronium and two for chloride, that have a similar magnitude as the profiles in Fig. 1(d). In contrast, the chloride peak is slightly higher than the hydronium one and is closer to it.

The density profiles with respect to the WCI at the interface with air are rather similar to the profiles at the interface with graphene [see Figs. 1(d) and 1(e)]. In both cases, the ionic GDS $z^{\mathrm{ions}}_{\mathrm{GDS}}$, obtained using the ionic density in Eq. (1), shown by vertical red dashed lines in Fig. 1, is to the right of the solution GDS, indicating a positive ionic surface excess.

We now look into the orientation of hydronium and water at these two interfaces. As shown in Fig. 1(f), the hydronium ions at the interface are strongly oriented with their three hydrogens pointing toward the water phase, i.e., $\cos(\theta_{H_3O^+}) \sim -1$, in agreement with previous studies.[10,15,54] This orientation is favored by the donation of three hydrogen bonds (HB) to the water molecules or to a chloride ion placed deeper in the liquid phase, as shown later in Fig. 6(d).

In addition, we overlay in orange in Figs. 1(c), 1(e), and 1(f) the results for the hydronium ion from the single ion pair simulations, where the H_3O^+ ion is initially placed at the interface (see Sec. S1 of the supplementary material for details). We find these profiles to be consistent with the profiles at high concentrations. In particular, the strong orientation at the interface is recovered both at the interface with graphene and at the interface with air. Note that the single-ion density profiles are not normalized since in this case the bulk density is zero, but their scale is adjusted to match the peak height of the concentrated simulations.

To investigate the water orientation, we develop an analysis based on Euler angles, described in Sec. S3 of the supplementary material, which allows us to plot the probability density of a given orientation, normalized by its probability in the isotropic bulk case. In Figs. 1(g) and 1(h), we show the profiles as a function of the distance to the WCI for two water orientations, which are selected because they exhibit a significant difference between the air and graphene interfaces. These are not the only relevant interfacial orientations at the interface; the full analysis is given in Sec. S3 of the supplementary material. In Figs. 1(g) and 1(h), we add sketches of the water molecules to visualize these orientations, where the oxygen is in red and the hydrogens are in white, and we indicate the directions of the two lone pairs as blue sticks. In the orientation analyzed in Fig. 1(g), one of the lone pairs of the water oxygen atom points away from the water phase. We observe oscillations in the probability profile for both interfaces, corresponding to the different water layers, with an increase in the portion of dangling lone pair configurations close to the WCI. The corresponding number density profiles as a function of the distance to the WCI are shown in Fig. S3 of the supplementary material and show that the density maxima of the first water layer are approximately at the same position for both interfaces, but the width of the peak is larger for the interface with air than with graphene. In particular, Fig. 1(g) shows that the water molecules closest to the interface with air show a different orientation and the portion of configurations with a lone pair pointing away from the water phase drops. Instead, as shown in Fig. 1(h), the ratio of configurations with two lone pairs parallel to the interface increases for the water molecules closest to the interface with air compared to the bulk. This difference in molecular

orientations of the last layer of water at the interface with air compared to graphene is interesting, considering that these two interfaces are often presented as very similar. It could be attributed to a specific interaction of the lone pair of water with graphene, or to the different interfacial stiffnesses: graphene is a rather stiff and flat interface, while the interface with air is rougher and more flexible.

INTERFACE PROPENSITY OF HYDROXIDE OH^-

We perform the same analysis for the concentrated NaOH electrolyte. At both interfaces, as shown in Figs. 2(c)–2(e), we observe a pronounced depletion of ions, with an ionic GDS located to the left of the solution GDS. At the interface with air, the density profiles plotted with respect to the WCI, shown in Fig. 2(d), show two hydration layers in the water profile, similarly to the HCl case. However, the ionic profiles show significant differences with respect to the HCl electrolyte. The sodium profile displays a monotonic sigmoidal shape with no preferential position, and no sodium ion is found in the first hydration layer, while we find a small population of hydroxide ions at the interface. Note that these results differ from previous FF-MD simulations at low concentrations[11] that show no hydroxide at all in the first hydration shell, but agree with the recent neural network based FF-MD of Litman *et al.*[50]

At the interface with graphene, shown in Fig. 2(e), we observe a layering of the water molecules, accompanied by a layering of the ionic densities. Although we have an overall ionic surface depletion, we observe a pronounced peak in the hydroxide density in the first hydration layer at the graphene surface. We also observe a small population of sodium ions at the interface, probably due to the high local concentration of anions. In Figs. 2(e) and 2(f), we additionally show as a broken cyan line the density and orientation profiles of hydroxide from the single ion-pair simulations, where one H_3O^+ and one OH^- are initially placed adsorbed on either side of a graphene sheet, as far away from each other in the xy plane as possible. The transient density profile shows a peak that coincides with the first hydration layer, as well as a long tail corresponding to ions diffusing away from the graphene sheet. Given that this density profile is an average over several simulations of about 6 ps (see Sec. S1 of the supplementary material for individual trajectories), such a large proportion of hydroxide ions diffusing away from the surface indicates a weak binding to the interface and a low barrier. In comparison, the DFT-MD study from Grosjean *et al.*,[70] based on a single hydroxide ion close to a graphene sheet and biased using umbrella sampling potentials, found a huge stabilization of the hydroxide ion at the graphene interface of about 11 k_BT without energy barrier between the bulk and the physisorbed state. This is quantitatively inconsistent with the potentials of mean force (PMF) obtained from our concentrated NaOH simulations, which suggest a barrier height of about 2.5 k_BT and a stabilization of only 0.5 k_BT with respect to the bulk (see Sec. S4 of the supplementary material for the PMF of all systems), as well as with the dynamics of our single ion pair simulations. We support this statement in Sec. S5 of the supplementary material, where we estimate characteristic times for escape from the interface from transition state theory as a function of the barrier height. In particular, we show that the frequency of the escape of hydroxide ions from the graphene surface, shown in Sec. S1 of the supplementary material as well as in Supplementary Movie 2 of Ref. 70, is incompatible with an interfacial adsorption free energy of 11 k_BT.

In Fig. 2(f), we show that both at the air and at the graphene interfaces, the hydroxide ion is strongly oriented with the hydrogen pointing away from the water phase, i.e., $\cos(\theta_{OH^-}) \sim +1$, as also found in Ref. 70. This is confirmed by our single ion-pair simulations.

Finally, the orientation of the water molecules at the interface with air and graphene, shown in Figs. 2(g) and 2(h), displays the same structure as for the HCl concentrated system, with the same differences between graphene and air. In addition, we note that the propensity for the dangling lone pair configuration is smaller in the NaOH system than in the HCl system. This can be correlated with the strong orientation of the hydronium ions, which in turn donate hydrogen bonds toward the water bulk, leading to a higher proportion of dangling lone pairs in the first hydration shell for HCl with respect to NaOH or pure water.

CONCENTRATION DEPENDENCE

The concentrations used in the DFT-MD simulations are very high. To investigate the influence of concentration on our results, we employ methods that require less computation time than DFT. One possibility is using analytical theories that describe the liquid structure, which we will discuss, but which we found do not allow a quantitative description of the high concentrations in our systems. Another possibility is to run FF-MD simulations, for which we can converge density profiles at any concentration. The challenge is to find a force field that correctly describes these systems. In a nutshell, we use a flexible force field for graphene combining intramolecular parameters from Ref. 92 and intermolecular parameters from Ref. 75. For the ions, we use the force field optimized by Bonthuis *et al.*[78] For the hydroxide ion, we modify the model by adding a partial charge on the hydrogen atom to give a dipole moment to the ion and we re-optimize the force field to reproduce the solvation free energy of NaOH at infinite dilution and the activity coefficients of NaOH solutions up to 9 mol/l. For the systems with a graphene sheet, we also optimize the intermolecular parameters between the ions and the carbon atoms. A full discussion of the force field optimization is given in Sec. S6 of the supplementary material.

To do a thorough analysis, we run a range of FF-MD simulations at different concentrations between 0.05 and 10 mol/l. All simulation details are given in Sec. S6 of the supplementary material, and only results for the lowest concentration and for the concentration closest to the DFT system are shown in Figs. 3 and 4. We show ionic density profiles in panels (a) and (d), ion orientation profiles in panels (b) and (e), as well as electric displacement field D_z/ϵ_0 profiles in panels (c) and (f), calculated from the ionic charge density profile $\rho_c(z) = \rho_+(z) - \rho_-(z)$ as

$$D_z(z) = \int_{L_z/2}^{z} \rho_c(z')\mathrm{d}z', \tag{2}$$

with $\rho_+(z)$ and $\rho_-(z)$ being the cation and anion density profiles. The same procedure is also used for the DFT-MD simulations. The integration of the displacement field yields ionic electrochemical potential profiles, which can be compared in a first approximation

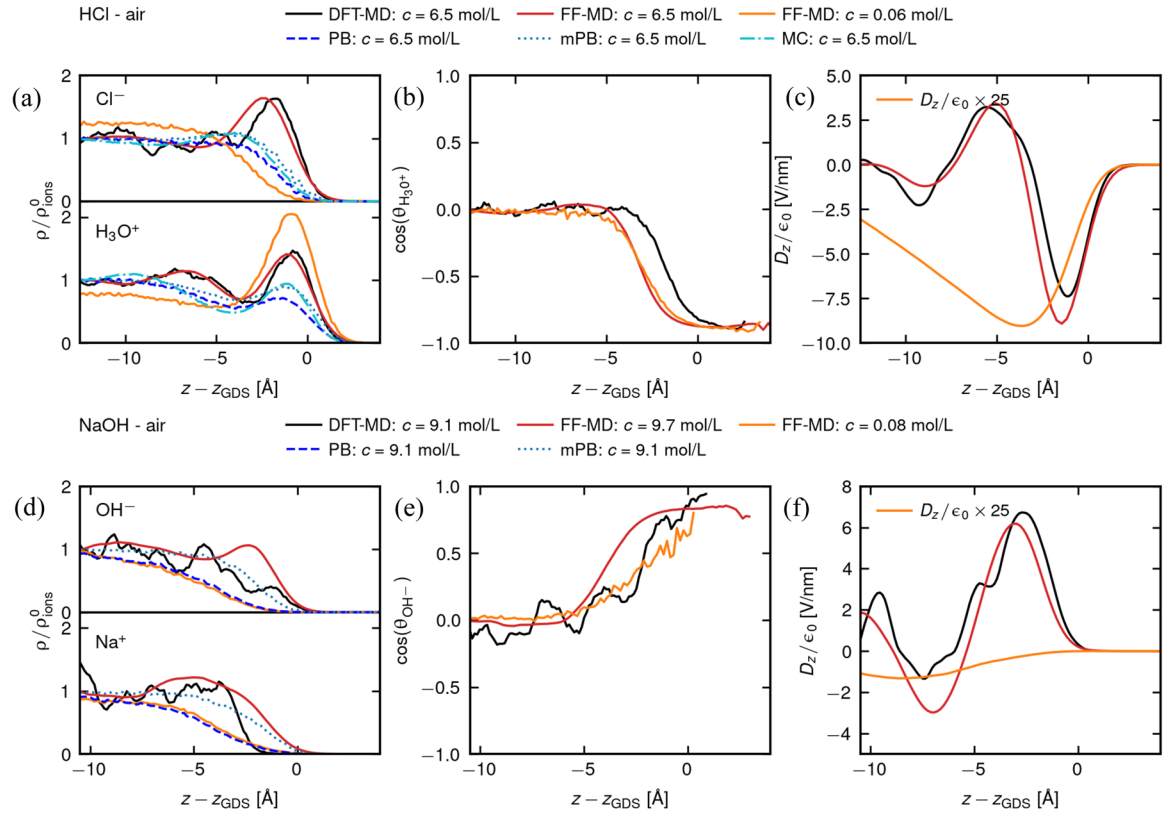

FIG. 3. Ionic density profiles for the HCl–air interface (a) and the NaOH–air interface (d), normalized by the ionic bulk density ρ^0_{ions}. Orientation profiles for the hydronium ion (b) and the hydroxide ion (e), as well as electric displacement field profiles [(c) and (f)] for the same systems. The profiles are shown as a function of the distance to the GDS. Data are shown for the DFT-MD simulations (black solid lines), for the FF-MD simulations at a similarly high concentration (red solid lines), and for the FF-MD simulations at low concentrations (orange solid lines). For the low concentration, electric displacement fields are multiplied by 25 for better readability [orange lines in panels (c) and (f)]. Predictions using the Poisson–Boltzmann (PB) equation (blue dashed lines) and the modified Poisson–Boltzmann (mPB) equation using an ion size of 4.3 Å (blue dotted lines) are also shown for comparison. For the HCl–air system, results from Monte Carlo (MC) simulations are also plotted (cyan dotted-dashed lines).

to electrokinetic potentials and ζ potential measurements,[38] which will be discussed in Fig. 5(c).

In Figs. 3(a)–3(c) and 4(a)–4(c), we find good agreement for the HCl electrolytes between the DFT-MD reference profiles (black solid lines) and the FF-MD results at a similar concentration (red solid lines) for both interfaces. Remarkably, the orientation profiles of hydronium in Figs. 3(b) and 4(b) are very well reproduced. We note that for the HCl–air interface, the orientation profile for the FF-MD in Fig. 3(b) is shifted with respect to the DFT-MD, which we attribute to the shift in the electric displacement field profile in Fig. 3(c), related to small shifts in the charge density profile. When extrapolating to low concentration [<0.1 mol/l, orange lines in Figs. 3(a)–3(c) and 4(a)–4(c)], we find that the hydronium density peak stays constant at the graphene interface and slightly increases at the interface with air. Meanwhile, the density peak of the chloride profiles disappears (only a small shoulder remains close to the graphene interface), which reflects the increased Debye–Hückel screening length of $\lambda_{\text{DH}} \approx 1$ nm for $c = 0.06$ mol/l. The strong orientation profiles are not modified by the concentration, showing that the interfacial hydronium orientation is driven by ion–water interactions and that collective ion effects are negligible. The electric displacement profiles in Figs. 3(c) and 4(c) depend on the relative concentration of cations and anions as a function of position, showing good agreement between the DFT-MD and FF-MD simulations at high concentrations at the interface with air. At the interface with graphene for DFT-MD simulations, due to an almost complete cancellation of the chloride and hydronium density peaks, we observe only a small negative peak in the D_z profile, while the density peaks in the FF-MD simulations are further apart, leading to a stronger negative contribution. This presumably is due to limitations of our ion-graphene force field.

For NaOH, the ionic density profiles from DFT-MD (black solid lines) and FF-MD (red solid lines) at high concentrations in Figs. 3(d) and 4(d) do not agree as well as for HCl, nevertheless, we obtain good agreement for the orientation and electric displacement field profiles in Figs. 3(e), 3(f), 4(e), and 4(f). The modification of the original force field[78] by adding a dipole moment to the hydroxide ion results in a good description of the strong orientation of hydroxide ions at both interfaces, as shown in Figs. 3(e) and 4(e). Although the results need to be interpreted with care, because of the limited agreement of density profiles at high concentrations with the DFT-MD simulations, we, nevertheless, consider the results obtained with

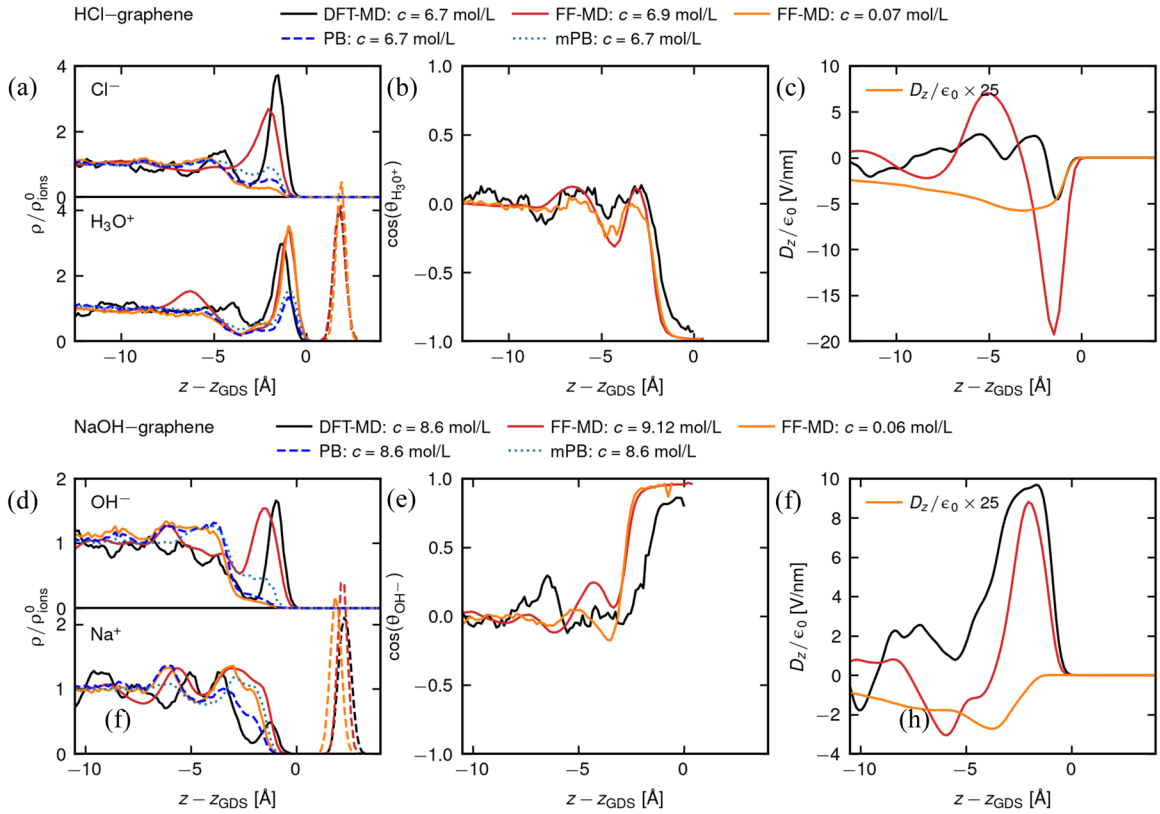

FIG. 4. Ionic density profiles for the HCl–graphene interface (a) and the NaOH–graphene interface (d), normalized by the ionic bulk density ρ^0_{ions}. The carbon density profile, arbitrarily normalized, is shown in dashed lines for reference. Orientation profiles for the hydronium ion (b) and the hydroxide ion (E), as well as electric displacement field profiles [(c) and (f)] for the same systems. The profiles are shown as a function of the distance to the GDS. Data are shown for the DFT-MD simulations (black solid lines), for the FF-MD simulations at a similarly high concentration (red solid lines), and for the FF-MD simulations at low concentrations (orange solid lines). For the low concentration, electric displacement fields are multiplied by 25 for better readability [orange lines in panels (c) and (f)]. Predictions using the Poisson–Boltzmann (PB) equation (blue dashed lines) and the modified Poisson–Boltzmann (mPB) equation using an ion size of 4.3 Å (blue dotted lines) are also shown for comparison.

this force field to be representative of the potential impact of concentration on our results. In Fig. 4(e), we observe that the strong orientation of hydroxide ions at the graphene interface is independent of concentration, while Fig. 3(e) at the interface with air shows a small concentration dependence, with a slightly weaker orientation at lower concentrations. Contrary to the HCl case, however, in the limit of low concentration, the small peak in the hydroxide density profile at the NaOH–air interface disappears completely and the large peak at the NaOH–graphene interface is drastically reduced [see the orange solid lines in Figs. 3(d) and 4(d)].

To compare these results with experimental data, in particular to confirm the validity of the density profiles, we calculate the difference in surface tension as a function of bulk ionic concentration ρ^0_{ions}. The Gibbs isotherm results in a relation between the derivative of the surface tension with respect to concentration and the ionic interfacial excess given by[11]

$$\frac{\mathrm{d}\gamma}{\mathrm{d}\rho^0_{\text{ions}}} = -2k_{\text{B}}T\left(z^{\text{ions}}_{\text{GDS}} - z^{\text{water}}_{\text{GDS}}\right)\frac{\mathrm{d}\ln a_{\pm}}{\mathrm{d}\ln \rho^0_{\text{ions}}}, \tag{3}$$

where $z^{\text{ions}}_{\text{GDS}} - z^{\text{water}}_{\text{GDS}}$ is the difference between the GDS of the ions and that of the water, defined in Eq. (1), and is proportional to the ionic excess, and $a_{cc} = \mathrm{d}\ln a_{\pm}/\mathrm{d}\ln\rho^0_{\text{ions}}$ is the log–log derivative of the mean activity coefficient of the salt $a_{\pm} = \sqrt{a_+ a_-}$. Note that the water GDS is close to the solution GDS. At low concentrations, a_{cc} is close to 1, but it increases for larger concentrations. Therefore, because of the high concentrations used in this work, we include the explicit concentration dependence of the experimental activity coefficient, using the experimental data from Hamer and Wu.[93] Note that the ionic force fields used were optimized to reproduce these experimental activity coefficients,[78] while it is computationally too expensive to calculate a_{cc} for the DFT simulations. We further consider the change in surface tension given by the integral

$$\Delta\gamma(\rho^0_{\text{ions}}) = \gamma(\rho^0_{\text{ions}}) - \gamma^0 = \int_0^{\rho^0_{\text{ions}}} \frac{\mathrm{d}\gamma(\rho^0)}{\mathrm{d}\rho^0}\mathrm{d}\rho^0, \tag{4}$$

where γ^0 is the pure water-interface surface tension and $\gamma(\rho^0_{\text{ions}})$ is that at finite concentrations. In Fig. 5(a), we show results for both the graphene interface $\Delta\gamma^{\text{graph}}$ (triangles) and the interface with

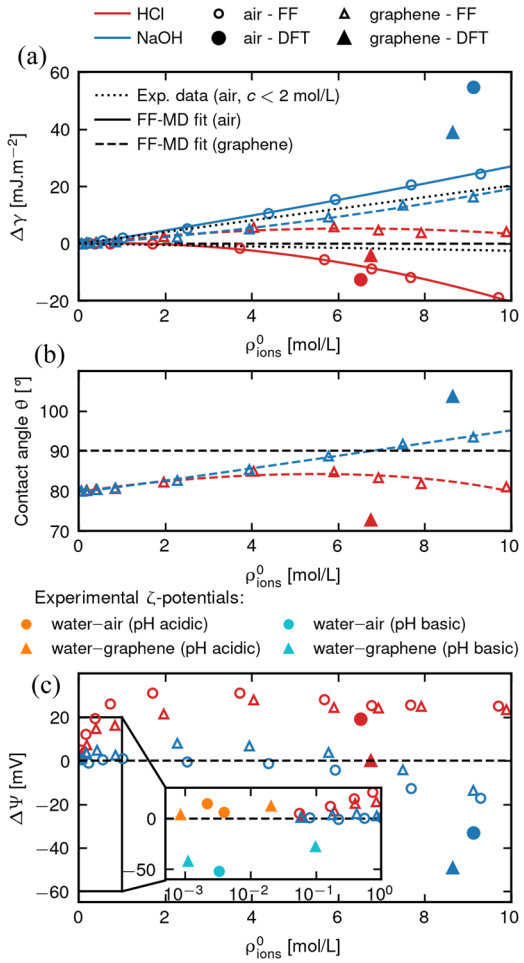

FIG. 5. (a) Surface tension change $\Delta\gamma$ as a function of concentration, given in Eq. (4). Data are shown for DFT-MD simulations (filled symbols) and FF-MD simulations (empty symbols), for the HCl (red symbols) and NaOH electrolytes (blue symbols) at the interface with air $\Delta\gamma^{air}$ (circles) and graphene $\Delta\gamma^{graph}$ (triangles). Quadratic fits to the FF-MD data are shown for HCl (red lines) and NaOH (blue lines) at the interface with air (solid lines) and graphene (dashed lines). The parameters are $\Delta\gamma = -0.01 + 0.35\rho - 0.24\rho^2$ for HCl–air, $\Delta\gamma = -0.27 + 1.76\rho - 0.14\rho^2$ for HCl–graphene, $\Delta\gamma = -0.36 + 2.40\rho + 0.03\rho^2$ for NaOH–air, and $\Delta\gamma = -0.30 + 1.11\rho + 0.08\rho^2$ for NaOH–graphene. Experimental data from Henry *et al.*[22] for the air–water interface are shown for comparison as black dotted lines. Note that the measurements were taken at relatively low concentrations, from 0.5 to 2 mol/l. (b) Contact angle of HCl and NaOH on graphene as a function of concentration, estimated from $\Delta\gamma$ using Young's equation (5). (c) Surface potential $\Delta\Psi$, defined in Eq. (6) as a function of concentration. In the inset, experimental ζ-potentials for air–water (filled circles) and graphene–water (filled triangles) for acidic solutions (orange symbols) and basic solutions (cyan symbols) are shown.[28,29,71,72]

air $\Delta\gamma^{air}$ (circles), extracted from DFT-MD simulations as well as from FF-MD simulations at a range of concentrations, compared with experimental data for the air–water interface.[22] For the FF-MD simulations, we find a mostly linear dependence of the surface tension on concentration, as observed experimentally,[22] with deviations above 5 mol/l. The full range of concentrations is best fitted using a quadratic function, shown as solid and dashed lines in Fig. 5(a) (parameters are given in the legend). For HCl, the DFT-MD results agree well with the experimental data, while for NaOH, they are larger. Note that the experimental data were measured for relatively dilute electrolytes, up to 2 mol/l. We further estimate the change in contact angle θ of HCl and NaOH electrolytes in contact with graphene as a function of concentration using Young's equation,

$$\cos\,\theta(\rho^0_{\text{ions}}) = \frac{\gamma^{\text{LV}}\cos\theta^0 - \Delta\gamma^{\text{graph}}(\rho^0_{\text{ions}})}{\gamma^{\text{LV}} + \Delta\gamma^{\text{air}}(\rho^0_{\text{ions}})}, \tag{5}$$

where $\gamma^{\text{LV}} = 63.6$ mJ m^{-2} is the liquid–vapor surface tension of pure SPC/E water[94] and $\Delta\gamma^{\text{graph}}$ and $\Delta\gamma^{\text{air}}$ are the changes in liquid–graphene and liquid–air surface tension, respectively, as a function of concentration, obtained from Eq. (4). Note that the graphene–air surface tension cancels out. We take the contact angle of pure SPC/E water on graphene to be $\theta^0 = 80°$.[75] The results are shown in Fig. 5(b). We find only a small change with concentration up to 5° for HCl electrolytes, while the contact angle increases to 95° for NaOH at 10 mol/l. DFT-MD simulations even predict a contact angle of 103° at a high concentration of NaOH, against 72° for highly concentrated HCl. The FF-MD results suggest that graphene becomes less hydrophilic as either of the water ions' concentration increases, with a transition to being hydrophobic ($\theta > 90°$) for highly basic solutions. For highly acidic solutions, it seems that graphene becomes more hydrophilic.

Next, we calculate the ionic electrostatic potential from the integral of the electric displacement field, given in Eq. (2), as

$$\Psi(z) = \frac{1}{\epsilon\epsilon_0}\int_{L_z/2}^{z} D_z(z')\mathrm{d}z', \tag{6}$$

with ϵ being the water dielectric constant. In Fig. 5(c), we plot surface potentials $\Delta\Psi = \Psi(L_z)$ relative to the pure water potential as a function of the ionic bulk density. These can be compared to electrokinetic measurements of the ζ-potential,[38] which is the electrostatic potential at the shear plane. We cannot obtain the position of the shear plane from our DFT-MD simulations; therefore, the electrostatic potential in vacuum is used as a reference in Eq. (6). To the best of our knowledge, no ζ-potential measurement at the air–water nor at the graphene–water interface at such high ion concentrations was reported in the literature. Experimental data for pH values between 2 and 12 are shown in Sec. S9 of the supplementary material.[28–30,71,72] In the inset of Fig. 5(c), we report the experimental ζ-potentials for the lowest pH at $\rho_{H_3O^+} = 10^{-\text{pH}}$ (orange symbols) and for the highest pH at $\rho_{OH^-} = 10^{-14+\text{pH}}$ (cyan symbols) at both the interface with air[28,29] and the interface with graphene:[71,72] for low pH, we find reasonable agreement with the experimental surface potentials of around 10 mV, while at high pH, our simulations give a surface potential close to zero and do not reproduce the highly negative experimental values. This reinforces the interpretation that negative ζ-potentials are not due to hydroxide adsorption but might be related to negatively charged contaminant molecules.[36] In addition, we note that the pH-dependent experimental data in Sec. S9 of the supplementary material show very similar ζ-potentials at the interface with air and graphene: the same is true for the values reported in Fig. 5(c), although larger deviations are found for DFT-MD simulations. Our FF-MD results also show a saturation for the

HCl electrolyte for concentrations higher than 3 mol/l, after which the surface potential reaches a plateau around 25 mV. On the contrary, for the NaOH electrolytes, we observe a small surface potential until a threshold of 6 mol/l, after which $\Delta\Psi$ decreases to −33 and −50 mV for the DFT-MD simulations and to −20 mV for FF-MD.

MOLECULAR INTERPRETATION

To interpret these results further, we investigate two analytical theories: we study the Poisson–Boltzmann (PB) equation including ion-specific ion–interface interactions,[95–98] as well as a modified Poisson–Boltzmann (mPB) equation that additionally takes into account the finite size of ions.[99,100] The details of the theory and methods used are given in Sec. S7 of the supplementary material. The PB theory considers point-like ions in solution, neglecting non-electrostatic interactions and ionic correlations. This approximation is typically good in the case of infinite dilution, but becomes significantly less accurate at higher concentrations. Taking into account the finite size of ions allows us to avoid unphysically high concentrations at charged surfaces and to describe the electric double layer formed at higher concentrations, going toward the modeling of ionic liquids.[99,100] Here, we first test these analytical theories against the FF-MD simulations. We use the ionic density profiles from FF-MD of the low concentration systems (orange lines in Figs. 3 and 4) to define potentials of mean force $U_{\pm}^{\mathrm{PMF}}(z) = -k_{\mathrm{B}}T \ln\left(\rho_{\pm}(z)/\rho_{\mathrm{ions}}^{0}\right)$ and predict the ionic densities at higher concentrations. By construction, the PB and FF-MD results agree for low concentrations. The full results are given in Sec. S7 of the supplementary material. From these, we find that for all systems, the PB equation taking into account only the PMF does not reproduce the features of the FF-MD density profiles at high concentrations. This can be seen in Figs. 3 and 4 by comparing the concentrated FF-MD results (red solid lines) with the PB predictions (blue dashed lines). The deviation between FF-MD and PB starts from concentrations of about 1–2 mol/l (see Figs. S24–S27 of the supplementary material). Introducing a correction to take into account the finite size of the ions leads to a slightly better description of the accumulation of ions at the interface, as seen by comparing the concentrated FF-MD results (red solid lines) with the mPB predictions (cyan dotted lines) in Figs. 3 and 4. For the NaOH–air interface, the mPB equation describes almost quantitatively the FF-MD results, except above 7–8 mol/l when specific adsorption to the surface is observed (see Fig. S26 of the supplementary material), but cannot describe the higher concentrations of the DFT-MD simulations in Fig. 3(d) (see cyan dotted lines compared to red solid lines). For the NaOH–graphene interface, however, where the adsorption of hydroxide at the interface in the FF-MD simulations at high concentrations is larger, the mPB theory describes the simulations well only up until 4 mol/l (see Fig. S27 of the supplementary material), but fails at describing the interfacial density peak in Fig. 4(d). For the HCl–air and HCl–graphene interfaces, we observe a strong adsorption of hydronium at both interfaces at all concentrations, which attracts chloride ions at high concentrations. This effect is reproduced by the mPB theory only qualitatively [see Figs. S24 and S25 of the supplementary material and Figs. 3(a) and 4(a)].

The discrepancies between analytical theories and MD results show that (i) ionic correlations, (ii) non-electrostatic interactions, and (iii) the molecular nature of these ions, in particular their dipole moment and their ability to form hydrogen bonds with the surrounding water molecules or other ions, play a crucial role at these interfaces. To investigate the impact of ionic correlations and non-electrostatic interactions, we performed Monte Carlo simulations of HCl systems modeled as point-like charges interacting with the surface via an ion–surface interaction $U_{\pm}^{\mathrm{PMF}}(z)$ and with each other via additional non-electrostatic ion–ion interactions determined from ionic correlations in the FF-MD simulations $U^{\mathrm{int}}(r)$. More details are given in Sec. S8 of the supplementary material. We find that these simulations have the same performance as the mPB theory with a finite ion size correction. Therefore, the peculiar behavior of hydroxide and hydronium is mainly due to the molecular nature of these ions.

To go deeper into the mechanism behind the strong orientation of these ions, we investigate the electrostatic fields created in different systems by different water orientations (around a neutral cavity, a charged cavity, and a molecular ion). For this, we investigate a single ion-pair at the air–water interface using FF-MD simulations, where the hydronium and hydroxide ion interactions with water are included on progressively more realistic levels. The three systems are schematized in Figs. 6(a)–6(c). In a first step, we include only the hydronium or hydroxide oxygen's LJ interaction, thereby creating a neutral cavity in the system. In a second step, we simulate a charged cavity, where we additionally include a point-charge of $q = \pm 1e$ on the hydronium or hydroxide oxygen atom. In the last step, we consider the full molecular ions as described by the force field optimized in Sec. S6 of the supplementary material. For each system, we run a 500 ns FF-MD simulation and extract the average z-component of the Coulomb force F_z^{C} acting on the hydronium or hydroxide oxygen atom as a function of its position, from which we calculate the electric field inside the oxygen cavity by $E_z = F_z^{\mathrm{C}}/q$. Note that, in practice, for the neutral cavity simulation, we use a small test charge of $q = 0.01e$ on the oxygen to calculate the Coulomb force on the linear-response level, and for all simulations, we adjust the charge of the counterion to enforce electroneutrality. The electric field profiles for the three systems are shown in Figs. 6(a)–6(c) for hydronium (red lines) and hydroxide (blue lines) ions. From these E_z profiles, we obtain the electric field at the oxygen position created by the surrounding water. These electric fields produce a force on the monopole charges: in the case of the E_z field produced in a neutral cavity (a), it is oriented such that positive charges are repelled from the interface and negative charges are attracted to the interface. In the case of a charged cavity (b), the electric field pushes both positive and negative ions away from the interface: this can be interpreted as an image charge effect at the interface between two dielectric media, where the dielectric constant of water is close to 80, while that of vacuum is 1. While these electric fields cannot explain the propensity of water ions for the interface, it has been proposed that they play a role for the water-ion orientation.[11] Indeed, the dipole–electric field interaction energy is given by $-\mu_z E_z$, where we take a dipole $\vec{\mu}$ to be oriented from the negative pole to the positive pole so that a positive electric field $E_z > 0$ applies a force on the dipole that would orient it with the positive pole pointing away from the water phase. In particular, for a small point-dipole $\vec{\mu}$ added in the neutral cavity, shown in Fig. 6(a), the water orientation at the interface and around the neutral cavity would cause the point-dipole to orient toward the bulk, since $E_z < 0$ at the interface. Note that we neglect here any image-dipole effects and that this result is consistent with the results

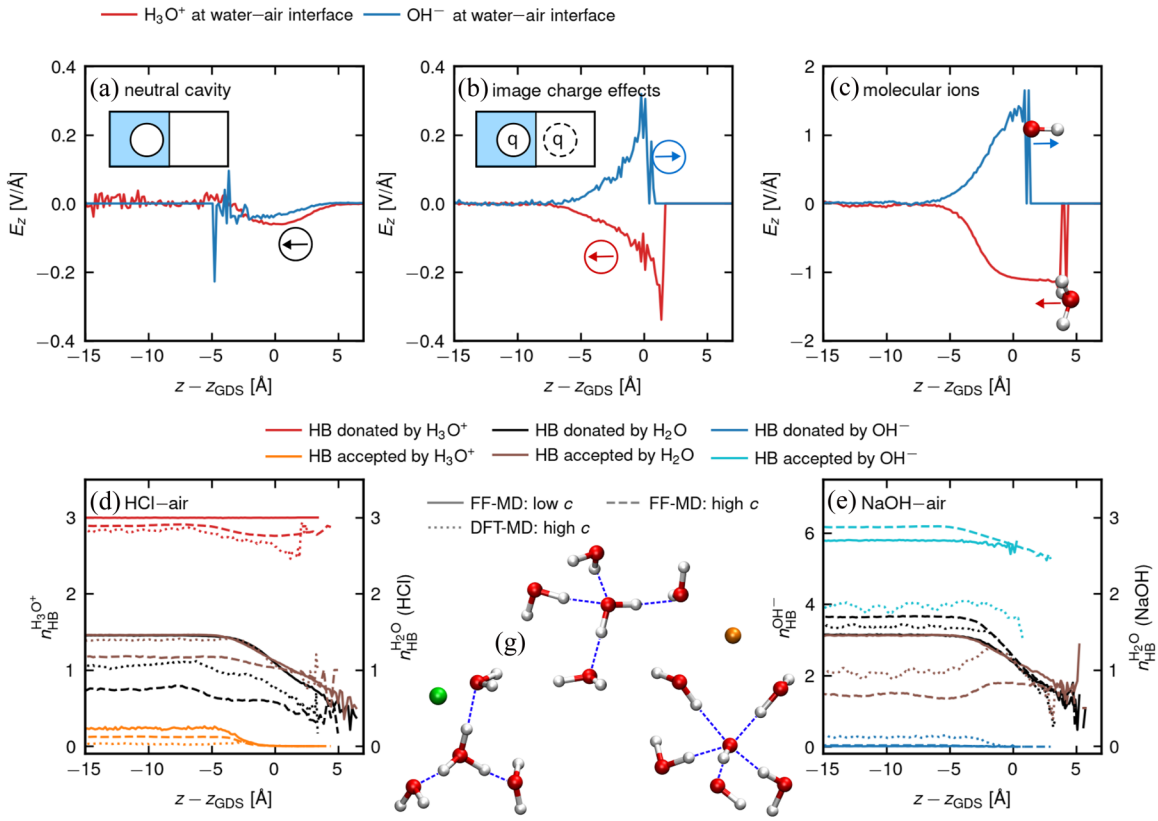

FIG. 6. (a)–(c) Electric field E_z at the oxygen position as a function of the distance to the GDS, calculated for a neutral cavity [(a), using the LJ parameters of the hydronium or the hydroxide oxygen atom], for a charged cavity [(b), $q = +1$ for the hydronium ion and $q = -1$ for the hydroxide ion], and for the molecular water ions (c). Simulations are run with a single ion pair in water at the interface with air (red solid line for hydronium and blue solid line for hydroxide). Refer to the main text for more details. (d) and (e) Number of hydrogen bonds as a function of the distance to the GDS for the HCl–air system (d) and the NaOH–air system (e). We distinguish hydrogen bonds donated by H_3O^+ (red lines), accepted by H_3O^+ (orange lines), donated by H_2O (black lines), accepted by H_2O (brown lines), donated by OH^- (blue lines), and accepted by OH^- (cyan lines). Data are shown for DFT-MD data (dotted lines) and for FF-MD simulations at low concentrations (solid lines) and at a high concentration similar to the DFT-MD one (dashed lines). Sketches of the hydration of water, hydronium, and hydroxide from DFT-MD simulations are shown, along with a chloride ion (green) and a sodium ion (orange).

obtained in Ref. 43 for an argon cavity. This is consistent with the H_3O^+ orientation but not with the OH^- opposite orientation seen in Fig. 2(f). For the charged cavity, shown in Fig. 6(b), we observe that the screening of the ion's charge by the water molecules around the cavity, corresponding to image charge effects, leads to a different orientation depending on the charge q of the cavity. Interestingly, the electric field profile in Fig. 6(b) shows that this imperfect screening leads to a preferential orientation of a point-dipole toward the bulk in case of a positive cavity corresponding to the hydronium ion and an orientation away from the bulk water in case of a negative cavity corresponding to the hydroxide ion. Finally, Fig. 6(c) shows the electric field profile felt at the ion's oxygen position due to the water orientation created in the presence of the molecular ions. This includes in particular the specific orientations due to hydrogen bonding. If we introduced a point-dipole at the position of the ions' oxygen, we would observe the same preferential orientations as predicted solely by the image charge effects in Fig. 6(b), which correspond to the water-ion orientations actually observed in the FF-MD simulations [see Figs. 3(b) and 3(e)]. However, the order of magnitude of the electric field in these three situations is very different: the electric field in the charged cavity is 4–5 times larger than that in the neutral cavity, meaning that the effect of the water orientation due to the interface is negligible with respect to the effect of the first solvation shell around a charged cavity. Moreover, the electric field in the system with molecular ions is 6–7 times larger than the one in the charged cavity. This means that the observed orientations of the hydronium ion toward the water phase and of the hydroxide ion away from it are predominantly due to hydrogen bonding and only to a smaller degree due to image charge effects.

To complete our analysis of how the molecular nature of the hydronium and hydroxide ions determines both the orientation and the propensity of the ions for the interface, we study the hydrogen bonding network as a function of position. We calculate the number of donated and accepted hydrogen bonds (HB) between a donor oxygen D and an acceptor oxygen or chloride A. We use a standard geometrical criterion to identify a hydrogen bond, i.e., the distance

$d_{DA} < 3.0$ Å and the angle $\theta_{HDA} < 30°$. The results are shown in Fig. 6(d) for the HCl–air interface, in Fig. 6(e) for the NaOH–air interface, and in Sec. S10 of the supplementary material for the interfaces with graphene, which show a similar behavior. Data are shown for DFT-MD simulations (dotted lines) and for FF-MD simulations at low concentrations (solid lines) and at high concentrations close to the DFT one (dashed lines). At low concentrations in bulk, we find as expected that water molecules donate 1.5 HB and receive 1.5 HB on average (black and brown solid lines). The hydronium ion donates three HB and receives on average 0.25 HB (red and orange solid lines), while the hydroxide ion donates no HB and receives 6 HB (cyan and blue solid lines). Note that this high number is not consistent with DFT data in the literature[101] and in our simulations [see the cyan dotted line in Fig. 6(e)], for which hydroxide receives only four HB, showing the limits of our force field for the hydroxide ion. Snapshots of the hydrogen bonding of a water molecule, a hydronium ion, and a hydroxide ion are shown in Fig. 6. Geometrical considerations can already give an intuitive explanation for the orientation of the hydronium and hydroxide ions at the interface. Indeed, due to the asymmetry of their hydrogen bonding patterns, maximizing the number of HB at the interface imposes that the hydronium ions point their hydrogens toward the water phase in order to donate three HB to the bulk water molecules, while the hydroxide ions point their oxygen atom toward the water phase, in order to maximize the number of accepted HB from the bulk water molecules.

For higher concentrations, we observe a modification of the water hydrogen bonding: in the concentrated HCl solution, the number of donated HB decreases to 0.75 in the FF-MD simulations and to 1.0 in the DFT-MD simulations [black dashed and dotted lines in Fig. 6(d)], which can be related to the presence of a large quantity of chloride ions, toward which water molecules orient their hydrogen atoms. On the contrary, in the concentrated NaOH solutions, the number of accepted HB decreases to 0.75 in the FF-MD simulations and to 1.0 in the DFT-MD simulations [brown dashed and dotted lines on the right axis in Fig. 6(e)], which can this time be related to the presence of a large quantity of sodium ions, toward which water molecules orient their oxygen atom.

As we approach the interface and the density decreases, we observe for both interfaces a decrease from 3 to 1 HB per water molecule, with a slight mismatch between the donated and accepted HB profiles (black and brown lines). Interestingly, in the case of HCl [see Fig. 6(d)], contrary to water molecules, the hydronium ion does not show a drastic decrease in HB at the interface: at low concentrations, the number of donated HB (red lines) stays constant to 3, and it only goes down to 2.5 for higher concentrations. Therefore, in agreement with previous work,[15,54] we propose that the strong propensity of hydronium ions for these interfaces at any ionic concentration is due to hydronium ions being less destabilized than water molecules at the interface, because their hydrogen bonding behavior is only slightly weakened (by the loss of 0.25 accepted HB) compared with the significant loss of 2 HB for an interfacial water molecule. In turn, donating three HB to the bulk water imposes a strong orientation of the hydronium ions toward the water phase, as observed in our simulations.

Following previous EXAFS and DFT studies on hydrochloric acid concentrated solutions,[102–104] we further investigate the solvation of chloride ions. We confirm the presence of a significant number of contact ion pairs H_3O^+–Cl^-, for which the chloride–hydronium distance is shorter than the chloride–water (H_2O–Cl^-) one, as demonstrated by the radial distribution functions (RDFs) in Sec. S11 of the supplementary material. In the case of sodium hydroxide, the number of contact ion pairs is small and no significant difference in the sodium–oxygen distances between OH^-–Na^+ and H_2O–Na^+ is observed. Results from FF simulations show good agreement with DFT ones, although the RDFs show a more structured liquid than in DFT. More interestingly, these RDFs also show the existence of non-dissociated molecular HCl species, with an H–Cl distance of 1.3 Å. These are by construction excluded from FF simulations. Stabilization of molecular HCl at the air–water has previously been reported in Ref. 104. The density profiles of molecular HCl from our DFT-MD simulations, shown in Fig. 7(a), confirm these findings: for both the HCl–air and HCl–graphene interfaces, molecular HCl is found mostly close to the interface. Our results suggest that stabilization of molecular HCl is a generic effect at hydrophobic interfaces.

For the NaOH electrolyte, shown in Fig. 6(e), we observe a peculiar behavior at high concentrations, in which the number of accepted HB by water molecules (brown dashed and dotted lines) slightly increases at the interface with respect to the value in bulk, which could be explained by a reduced concentration of sodium ions at the interface, allowing for more accepted HB. Apart from this, the HB profiles for NaOH do not explain the gradual increase in the OH^- density peak at the interface with increasing concentration, in particular at the interface with graphene, observed in FF-MD simulations. This concentration dependence, not observed in the case of HCl electrolytes, hints at a cooperative effect. Thus, in Sec. S12 of the supplementary material, we compute the radial distribution function for the hydroxide oxygen atoms in the first hydration layer at the graphene interface. For FF-MD, this pair correlation function shows a clear maximum at 4.4 Å, compared with 2.8 Å for the water oxygens. This maximum corresponds to configurations where two hydroxide ions are separated by a single water molecule, donating one HB to each hydroxide ion. Given that the hydroxide ions both orient in the same direction, this is a surprising configuration. Indeed, in usual electrostatics, we would expect two dipoles oriented in the same direction to be repelled by each other. This, therefore,

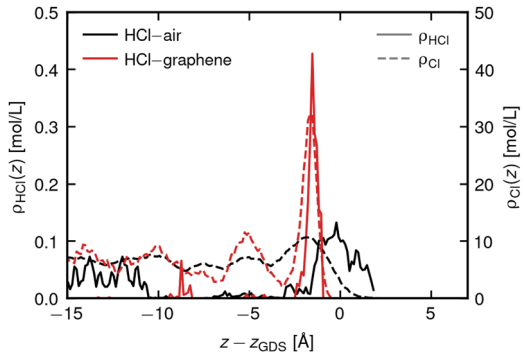

FIG. 7. Density of molecular HCl species (solid lines) and chloride atoms (dashed lines) as a function of the distance to the GDS. Data are shown for the DFT-MD simulations of concentrated HCl solutions at the interface with air (black lines) and with graphene (red lines).

points to a screening of the dipole moment by the rearrangement of water molecules around the hydroxide ion and to a favorable interaction between hydroxide ions mediated by hydrogen bonding. The radial distribution profile for DFT-MD shows a peak at the same position but not as high as for FF-MD. It is thus unclear whether this effect plays a role in the DFT-MD simulations or if it is only observed with the force field used. Given the limitations of our force field for hydroxide, in particular the discrepancies for the hydrogen bonding pattern with respect to DFT-MD at high concentrations, these FF-MD results should thus be merely considered as a starting point for more accurate investigations.

CONCLUSION

In this work, we performed extensive DFT-MD simulations of HCl and NaOH highly concentrated electrolytes at the interface with air and graphene. The large number of ions enables good sampling of phase space in the simulation times accessible by DFT. In addition, in order to obtain estimations for low concentrations, we performed DFT-MD simulations of single ion-pairs and we combined and adapted classical force fields to reproduce our DFT-MD simulations at high concentrations. The FF-MD simulations are rather reliable for the HCl systems, but for the NaOH systems, there are discrepancies in the density profiles and hydrogen bonding topologies at high concentrations, compared to DFT-MD results.

In agreement with surface tension measurements of acid and base interfaces with air,[22] we find that HCl has an ionic surface excess, while NaOH displays an ionic surface depletion, for both interfaces. We additionally predict a decreasing graphene hydrophilicity for increasing water ion concentration, with a transition to hydrophobic graphene for highly basic solutions. Finally, we find for both interfaces a positive surface potential for acids and an almost neutral surface potential for bases, which becomes negative only above ~7 mol/l.

At the molecular scale, we observe for HCl an adsorption of hydronium ions at both interfaces, roughly independent of concentration, that display a strong orientation with the three hydrogen atoms pointing toward the water phase. We demonstrate that this orientation is dictated by the hydrogen bonding behavior of hydronium ions, which donate three hydrogen bonds to the water molecules in bulk. We argue that the high propensity of hydronium ions for both interfaces with air and graphene, even at low concentrations, is due to the fact that hydronium ions retain their three donated hydrogen bonds even at the interface, while water molecules lose on average two hydrogen bonds at the interface, making it favorable to accumulate hydronium ions instead of water molecules at the interface.

For NaOH, although we find an overall ionic surface depletion, we observe density peaks for hydroxide at the interface with air and graphene from concentrated DFT-MD simulations, the latter inducing the largest density peak. At low concentrations, our FF-MD simulations predict a gradual disappearance of the density peak, suggesting no hydroxide adsorption in dilute systems. In addition, the hydroxide ions at the interface have a strong orientation, opposite to the one of hydronium, with their hydrogen pointing away from the water phase. We show that this orientation is due to the favorable hydrogen bonds accepted by OH^- from the bulk water molecules. The FF-MD simulations suggest a cooperative effect of neighboring aligned hydroxide ions, which will need to be confirmed in future studies.

This study highlights the molecular interfacial effects of the hydronium and hydroxide ions that are not captured by standard Poisson–Boltzmann theory. We also investigated the difference between the air–water and graphene–water interfaces. These two interfaces are commonly compared because of their similar effect on liquid water,[105,106] despite their different rigidity.[107] Through a careful analysis, we reveal subtle differences in the orientation of water molecules in the vicinity of the air–water and graphene–water interfaces. However these differences do not seem to have a significant effect on the hydrogen bonding patterns and their position dependence. The behavior of the water ions is also very similar at these two interfaces, with identical orientations of the hydroxide and hydronium ions and similar ionic density profiles at the interfaces. This results in similar trends in the surface tension and surface potential dependence on the water ion concentration.

SUPPLEMENTARY MATERIAL

The supplementary material contains additional simulation details, the definition of the Willard–Chandler interface, details on the orientation analysis, the force field optimization, as well as the full concentration-dependent results, details on the Poisson–Boltzmann theories, and the Monte Carlo simulations.

ACKNOWLEDGMENTS

We thank Marie-Laure Bocquet for fruitful discussions. We acknowledge the support provided by the European Research Council under the European Union's Horizon 2020 research and innovation program (Grant Agreement No. 835117) and the Deutsche Forschungsgemeinschaft, Grant Nos. CRC 1349 and 1078. Alexandre P. dos Santos acknowledges the Brazilian National Council for Scientific and Technological Development (CNPq) for the financial support under Grant No. 303463/2021-0. We acknowledge computing resources from the Hochleistungsrechenzentrum Norddeutschland, Project No. bep00106, as well as from the CURTA HPC cluster at ZEDAT, FU Berlin.[108]

AUTHOR DECLARATIONS

Conflict of Interest

The authors have no conflicts to disclose.

Author Contributions

Laura Scalfi: Conceptualization (equal); Investigation (equal); Methodology (equal); Software (equal); Validation (equal); Visualization (equal); Writing – original draft (equal). **Louis Lehmann**: Investigation (supporting); Methodology (supporting); Software (supporting); Writing – original draft (supporting). **Alexandre P. dos Santos**: Investigation (supporting); Software (supporting);

Writing – original draft (supporting). **Maximilian R. Becker**: Investigation (supporting); Methodology (supporting); Software (supporting); Visualization (supporting); Writing – original draft (supporting). **Roland R. Netz**: Conceptualization (equal); Investigation (equal); Methodology (equal); Supervision (equal); Writing – original draft (equal).

DATA AVAILABILITY

The data that support the findings of this study are available from the corresponding author upon reasonable request.

REFERENCES

[1]M. F. Ruiz-Lopez, J. S. Francisco, M. T. Martins-Costa, and J. M. Anglada, "Molecular reactions at aqueous interfaces," Nat. Rev. Chem. **4**, 459–475 (2020).

[2]A. M. Deal, R. J. Rapf, and V. Vaida, "Water–air interfaces as environments to address the water paradox in prebiotic chemistry: A physical chemistry perspective," J. Phys. Chem. A **125**, 4929–4942 (2021).

[3]Z. Guo, J. Huang, X. Dong, Y. Xia, L. Yan, Z. Wang, and Y. Wang, "An organic/inorganic electrode-based hydronium-ion battery," Nat. Commun. **11**, 959 (2020).

[4]A. J. Colussi, S. Enami, and S. Ishizuka, "Hydronium ion acidity above and below the interface of aqueous microdroplets," ACS Earth Space Chem. **5**, 2341–2346 (2021).

[5]C. Merlet, B. Rotenberg, P. A. Madden, P.-L. Taberna, P. Simon, Y. Gogotsi, and M. Salanne, "On the molecular origin of supercapacitance in nanoporous carbon electrodes," Nat. Mater. **11**, 306–310 (2012).

[6]L. Onsager and N. N. T. Samaras, "The surface tension of Debye-Hückel electrolytes," J. Chem. Phys. **2**, 528–536 (1934).

[7]V. Buch, A. Milet, R. Vácha, P. Jungwirth, and J. P. Devlin, "Water surface is acidic," Proc. Natl. Acad. Sci. U. S. A. **104**, 7342–7347 (2007).

[8]F. Giberti and A. A. Hassanali, "The excess proton at the air-water interface: The role of instantaneous liquid interfaces," J. Chem. Phys. **146**, 244703 (2017).

[9]H.-S. Lee and M. E. Tuckerman, "*Ab initio* molecular dynamics studies of the liquid–vapor interface of an HCl solution," J. Phys. Chem. A **113**, 2144–2151 (2009).

[10]A. P. dos Santos and Y. Levin, "Surface tensions and surface potentials of acid solutions," J. Chem. Phys. **133**, 154107 (2010).

[11]S. I. Mamatkulov, C. Allolio, R. R. Netz, and D. J. Bonthuis, "Orientation-induced adsorption of hydrated protons at the air-water interface," Angew. Chem., Int. Ed. **56**, 15846–15851 (2017).

[12]M. Mucha, T. Frigato, L. M. Levering, H. C. Allen, D. J. Tobias, L. X. Dang, and P. Jungwirth, "Unified molecular picture of the surfaces of aqueous acid, base, and salt solutions," J. Phys. Chem. B **109**, 7617–7623 (2005).

[13]P. Jungwirth and D. J. Tobias, "Specific ion effects at the air/water interface," Chem. Rev. **106**, 1259–1281 (2006).

[14]M. Becker, P. Loche, M. Rezaei, A. Wolde-Kidan, Y. Uematsu, R. R. Netz, and D. J. Bonthuis, "Multiscale modeling of aqueous electric double layers," Chem. Rev. **124**, 1–26 (2023).

[15]S. Iuchi, H. Chen, F. Paesani, and G. A. Voth, "Hydrated excess proton at water–hydrophobic interfaces," J. Phys. Chem. B **113**, 4017–4030 (2009).

[16]R. Kumar, C. Knight, and G. A. Voth, "Exploring the behaviour of the hydrated excess proton at hydrophobic interfaces," Faraday Discuss. **167**, 263–278 (2013).

[17]D. L. McCaffrey, S. C. Nguyen, S. J. Cox, H. Weller, A. P. Alivisatos, P. L. Geissler, and R. J. Saykally, "Mechanism of ion adsorption to aqueous interfaces: Graphene/water vs. air/water," Proc. Natl. Acad. Sci. U. S. A. **114**, 13369–13373 (2017).

[18]R. Zimmermann, U. Freudenberg, R. Schweiß, D. Küttner, and C. Werner, "Hydroxide and hydronium ion adsorption—A survey," Curr. Opin. Colloid Interface Sci. **15**, 196–202 (2010).

[19]R. Zangi and J. B. F. N. Engberts, "Physisorption of hydroxide ions from aqueous solution to a hydrophobic surface," J. Am. Chem. Soc. **127**, 2272–2276 (2005).

[20]R. J. Saykally, "Two sides of the acid–base story," Nat. Chem. **5**, 82–84 (2013).

[21]N. Agmon, H. J. Bakker, R. K. Campen, R. H. Henchman, P. Pohl, S. Roke, M. Thämer, and A. Hassanali, "Protons and hydroxide ions in aqueous systems," Chem. Rev. **116**, 7642–7672 (2016).

[22]C. L. Henry, C. N. Dalton, L. Scruton, and V. S. J. Craig, "Ion-specific coalescence of bubbles in mixed electrolyte solutions," J. Phys. Chem. C **111**, 1015–1023 (2007).

[23]Y. Marcus, "Surface tension of aqueous electrolytes and ions," J. Chem. Eng. Data **55**, 3641–3644 (2010).

[24]L. M. Pegram and M. T. Record, "Hofmeister salt effects on surface tension arise from partitioning of anions and cations between bulk water and the air–water interface," J. Phys. Chem. B **111**, 5411–5417 (2007).

[25]P. K. Weissenborn and R. J. Pugh, "Surface tension of aqueous solutions of electrolytes: Relationship with ion hydration, oxygen solubility, and bubble coalescence," J. Colloid Interface Sci. **184**, 550–563 (1996).

[26]P. Creux, J. Lachaise, A. Graciaa, and J. K. Beattie, "Specific cation effects at the hydroxide-charged air/water interface," J. Phys. Chem. C **111**, 3753–3755 (2007).

[27]P. Creux, J. Lachaise, A. Graciaa, J. K. Beattie, and A. M. Djerdjev, "Strong specific hydroxide ion binding at the pristine oil/water and air/water interfaces," J. Phys. Chem. B **113**, 14146–14150 (2009).

[28]M. Takahashi, "ζ potential of microbubbles in aqueous solutions: Electrical properties of the gas–water interface," J. Phys. Chem. B **109**, 21858–21864 (2005).

[29]C. Yang, T. Dabros, D. Li, J. Czarnecki, and J. H. Masliyah, "Measurement of the zeta potential of gas bubbles in aqueous solutions by microelectrophoresis method," J. Colloid Interface Sci. **243**, 128–135 (2001).

[30]C. Li and P. Somasundaran, "Reversal of bubble charge in multivalent inorganic salt solutions—Effect of magnesium," J. Colloid Interface Sci. **146**, 215–218 (1991).

[31]W. Gan, W. Wu, F. Yang, D. Hu, H. Fang, Z. Lan, and Q. Yuan, "The behavior of hydroxide and hydronium ions at the hexadecane–water interface studied with second harmonic generation and zeta potential measurements," Soft Matter **13**, 7962–7968 (2017).

[32]M. Manciu, F. S. Manciu, and E. Ruckenstein, "On the surface tension and Zeta potential of electrolyte solutions," Adv. Colloid Interface Sci. **244**, 90–99 (2017).

[33]R. Vácha, O. Marsalek, A. P. Willard, D. J. Bonthuis, R. R. Netz, and P. Jungwirth, "Charge transfer between water molecules as the possible origin of the observed charging at the surface of pure water," J. Phys. Chem. Lett. **3**, 107–111 (2012).

[34]E. Poli, K. H. Jong, and A. Hassanali, "Charge transfer as a ubiquitous mechanism in determining the negative charge at hydrophobic interfaces," Nat. Commun. **11**, 901 (2020).

[35]Y. Uematsu, D. J. Bonthuis, and R. R. Netz, "Impurity effects at hydrophobic surfaces," Curr. Opin. Electrochem. **13**, 166–173 (2019).

[36]Y. Uematsu, D. J. Bonthuis, and R. R. Netz, "Nanomolar surface-active charged impurities account for the zeta potential of hydrophobic surfaces," Langmuir **36**, 3645–3658 (2020).

[37]Y. Uematsu, D. J. Bonthuis, and R. R. Netz, "Charged surface-active impurities at nanomolar concentration induce Jones–Ray effect," J. Phys. Chem. Lett. **9**, 189–193 (2018).

[38]A. Wolde-Kidan and R. R. Netz, "Interplay of interfacial viscosity, specific-ion, and impurity adsorption determines zeta potentials of phospholipid membranes," Langmuir **37**, 8463–8473 (2021).

[39]B. Winter, M. Faubel, R. Vácha, and P. Jungwirth, "Behavior of hydroxide at the water/vapor interface," Chem. Phys. Lett. **474**, 241–247 (2009).

[40]J. K. Beattie, "Comment on 'Behaviour of hydroxide at the water/vapor interface' [Chem. Phys. Lett. 474 (2009) 241]," Chem. Phys. Lett. **481**, 17–18 (2009).

[41]B. Winter, M. Faubel, R. Vácha, and P. Jungwirth, "Reply to comments on Frontiers Article 'Behavior of hydroxide at the water/vapor interface'," Chem. Phys. Lett. **481**, 19–21 (2009).

[42]S. Pullanchery, S. Kulik, H. I. Okur, H. B. de Aguiar, and S. Roke, "On the stability and necessary electrophoretic mobility of bare oil nanodroplets in water," J. Chem. Phys. **152**, 241104 (2020).

[43]M. R. Becker, P. Loche, and R. R. Netz, "Electrokinetic, electrochemical, and electrostatic surface potentials of the pristine water liquid–vapor interface," J. Chem. Phys. **157**, 240902 (2022).
[44]P. B. Petersen and R. J. Saykally, "Evidence for an enhanced hydronium concentration at the liquid water surface," J. Phys. Chem. B **109**, 7976–7980 (2005).
[45]C. Tian, N. Ji, G. A. Waychunas, and Y. R. Shen, "Interfacial structures of acidic and basic aqueous solutions," J. Am. Chem. Soc. **130**, 13033–13039 (2008).
[46]L. M. Levering, M. R. Sierra-Hernández, and H. C. Allen, "Observation of hydronium ions at the air–aqueous acid interface: Vibrational spectroscopic studies of aqueous HCl, HBr, and HI," J. Phys. Chem. C **111**, 8814–8826 (2007).
[47]P. B. Petersen and R. J. Saykally, "Is the liquid water surface basic or acidic? Macroscopic vs. molecular-scale investigations," Chem. Phys. Lett. **458**, 255–261 (2008).
[48]T. L. Tarbuck, S. T. Ota, and G. L. Richmond, "Spectroscopic studies of solvated hydrogen and hydroxide ions at aqueous surfaces," J. Am. Chem. Soc. **128**, 14519–14527 (2006).
[49]S. Das, M. Bonn, and E. H. G. Backus, "The surface activity of the hydrated proton is substantially higher than that of the hydroxide ion," Angew. Chem., Int. Ed. **58**, 15636–15639 (2019).
[50]Y. Litman, K.-Y. Chiang, T. Seki, Y. Nagata, and M. Bonn, "Surface stratification determines the interfacial water structure of simple electrolyte solutions," Nat. Chem. **16**, 644–650 (2024).
[51]L. X. Dang, "Solvation of the hydronium ion at the water liquid/vapor interface," J. Chem. Phys. **119**, 6351–6353 (2003).
[52]M. D. Baer, I.-F. W. Kuo, D. J. Tobias, and C. J. Mundy, "Toward a unified picture of the water self-ions at the air–water interface: A density functional theory perspective," J. Phys. Chem. B **118**, 8364–8372 (2014).
[53]B. Jagoda-Cwiklik, L. Cwiklik, and P. Jungwirth, "Behavior of the Eigen form of hydronium at the air/water interface," J. Phys. Chem. A **115**, 5881–5886 (2011).
[54]J. S. Hub, M. G. Wolf, C. Caleman, P. J. van Maaren, G. Groenhof, and D. van der Spoel, "Thermodynamics of hydronium and hydroxide surface solvation," Chem. Sci. **5**, 1745–1749 (2014).
[55]M. K. Petersen, S. S. Iyengar, T. J. F. Day, and G. A. Voth, "The hydrated proton at the water liquid/vapor interface," J. Phys. Chem. B **108**, 14804–14806 (2004).
[56]Y.-L. S. Tse, C. Chen, G. E. Lindberg, R. Kumar, and G. A. Voth, "Propensity of hydrated excess protons and hydroxide anions for the air–water interface," J. Am. Chem. Soc. **137**, 12610–12616 (2015).
[57]C. D. Wick, "Hydronium behavior at the air–water interface with a polarizable multistate empirical valence bond model," J. Phys. Chem. C **116**, 4026–4038 (2012).
[58]C. D. Wick, "Comparing hydroxide and hydronium at the instantaneous air-water interface using polarizable multi-state empirical valence bond models," Comput. Theor. Chem. **1116**, 64–72 (2017).
[59]C. J. Mundy, I.-F. W. Kuo, M. E. Tuckerman, H.-S. Lee, and D. J. Tobias, "Hydroxide anion at the air–water interface," Chem. Phys. Lett. **481**, 2–8 (2009).
[60]C. Bai and J. Herzfeld, "Surface propensities of the self-ions of water," ACS Cent. Sci. **2**, 225–231 (2016).
[61]M. de la Puente and D. Laage, "How the acidity of water droplets and films is controlled by the air–water interface," J. Am. Chem. Soc. **145**, 25186–25194 (2023).
[62]T. Mouterde, A. Keerthi, A. R. Poggioli, S. A. Dar, A. Siria, A. K. Geim, L. Bocquet, and B. Radha, "Molecular streaming and its voltage control in ångström-scale channels," Nature **567**, 87–90 (2019).
[63]T. Emmerich, K. S. Vasu, A. Niguès, A. Keerthi, B. Radha, A. Siria, and L. Bocquet, "Enhanced nanofluidic transport in activated carbon nanoconduits," Nat. Mater. **21**, 696–702 (2022).
[64]P. Dhiman, F. Yavari, X. Mi, H. Gullapalli, Y. Shi, P. M. Ajayan, and N. Koratkar, "Harvesting energy from water flow over graphene," Nano Lett. **11**, 3123–3127 (2011).
[65]D. B. Shinde, I. V. Vlassiouk, M. R. Talipov, and S. N. Smirnov, "Exclusively proton conductive membranes based on reduced graphene oxide polymer composites," ACS Nano **13**, 13136–13143 (2019).
[66]L. Madauß, T. Foller, J. Plaß, P. V. Kumar, T. Musso, K. Dunkhorst, R. Joshi, and M. Schleberger, "Selective proton transport for hydrogen production using graphene oxide membranes," J. Phys. Chem. Lett. **11**, 9415–9420 (2020).
[67]B. R. H. de Aquino, H. Ghorbanfekr-Kalashami, M. Neek-Amal, and F. M. Peeters, "Ionized water confined in graphene nanochannels," Phys. Chem. Chem. Phys. **21**, 9285–9295 (2019).
[68]H. Duan, Z. Ying, L. Tian, Y. Cheng, and L. Shi, "Aqueous proton transportation in graphene-based nanochannels," Langmuir **38**, 15413–15421 (2022).
[69]B. Grosjean, C. Pean, A. Siria, L. Bocquet, R. Vuilleumier, and M.-L. Bocquet, "Chemisorption of hydroxide on 2D materials from DFT calculations: Graphene versus hexagonal boron nitride," J. Phys. Chem. Lett. **7**, 4695–4700 (2016).
[70]B. Grosjean, M.-L. Bocquet, and R. Vuilleumier, "Versatile electrification of two-dimensional nanomaterials in water," Nat. Commun. **10**, 1656 (2019).
[71]C. Cui, J. Huang, J. Huang, and G. Chen, "Size separation of mechanically exfoliated graphene sheets by electrophoresis," Electrochim. Acta **258**, 793–799 (2017).
[72]D. Li, M. B. Müller, S. Gilje, R. B. Kaner, and G. G. Wallace, "Processable aqueous dispersions of graphene nanosheets," Nat. Nanotechnol. **3**, 101–105 (2008).
[73]E. Mangaud, M.-L. Bocquet, L. Bocquet, and B. Rotenberg, "Chemisorbed vs physisorbed surface charge and its impact on electrokinetic transport: Carbon vs boron nitride surface," J. Chem. Phys. **156**, 044703 (2022).
[74]D. J. Cole, P. K. Ang, and K. P. Loh, "Ion adsorption at the graphene/electrolyte interface," J. Phys. Chem. Lett. **2**, 1799–1803 (2011).
[75]S. R. Carlson, O. Schullian, M. R. Becker, and R. R. Netz, "Modeling water interactions with graphene and graphite via force fields consistent with experimental contact angles," J. Phys. Chem. Lett. **15**, 6325–6333 (2024).
[76]B. Coquinot, M. Becker, R. R. Netz, L. Bocquet, and N. Kavokine, "Collective modes and quantum effects in two-dimensional nanofluidic channels," Faraday Discuss. **249**, 162–180 (2024).
[77]M. J. Abraham, T. Murtola, R. Schulz, S. Páll, J. C. Smith, B. Hess, and E. Lindahl, "GROMACS: High performance molecular simulations through multi-level parallelism from laptops to supercomputers," SoftwareX **1–2**, 19 (2015).
[78]D. J. Bonthuis, S. I. Mamatkulov, and R. R. Netz, "Optimization of classical nonpolarizable force fields for OH^- and H_3O^+," J. Chem. Phys. **144**, 104503 (2016).
[79]T. D. Kühne, M. Iannuzzi, M. Del Ben, V. V. Rybkin, P. Seewald, F. Stein, T. Laino, R. Z. Khaliullin, O. Schütt, F. Schiffmann, D. Golze, J. Wilhelm, S. Chulkov, M. H. Bani-Hashemian, V. Weber, U. Borštnik, M. Taillefumier, A. S. Jakobovits, A. Lazzaro, H. Pabst, T. Müller, R. Schade, M. Guidon, S. Andermatt, N. Holmberg, G. K. Schenter, A. Hehn, A. Bussy, F. Belleflamme, G. Tabacchi, A. Glöß, M. Lass, I. Bethune, C. J. Mundy, C. Plessl, M. Watkins, J. VandeVondele, M. Krack, and J. Hutter, "CP2K: An electronic structure and molecular dynamics software package - Quickstep: Efficient and accurate electronic structure calculations," J. Chem. Phys. **152**, 194103 (2020).
[80]A. D. Becke, "Density-functional exchange-energy approximation with correct asymptotic behavior," Phys. Rev. A **38**, 3098–3100 (1988).
[81]C. Lee, W. Yang, and R. G. Parr, "Development of the Colle-Salvetti correlation-energy formula into a functional of the electron density," Phys. Rev. B **37**, 785–789 (1988).
[82]S. Grimme, J. Antony, S. Ehrlich, and H. Krieg, "A consistent and accurate *ab initio* parametrization of density functional dispersion correction (DFT-D) for the 94 elements H-Pu," J. Chem. Phys. **132**, 154104 (2010).
[83]J. VandeVondele and J. Hutter, "Gaussian basis sets for accurate calculations on molecular systems in gas and condensed phases," J. Chem. Phys. **127**, 114105 (2007).
[84]S. Goedecker, M. Teter, and J. Hutter, "Separable dual-space Gaussian pseudopotentials," Phys. Rev. B **54**, 1703–1710 (1996).
[85]R. A. Kendall, T. H. Dunning, Jr., and R. J. Harrison, "Electron affinities of the first-row atoms revisited. Systematic basis sets and wave functions," J. Chem. Phys. **96**, 6796–6806 (1992).
[86]F. N. Brünig, M. Rammler, E. M. Adams, M. Havenith, and R. R. Netz, "Spectral signatures of excess-proton waiting and transfer-path dynamics in aqueous hydrochloric acid solutions," Nat. Commun. **13**, 4210 (2022).

[87]J. S. Hub, B. L. de Groot, H. Grubmüller, and G. Groenhof, "Quantifying artifacts in Ewald simulations of inhomogeneous systems with a net charge," J. Chem. Theory Comput. **10**, 381–390 (2014).
[88]J. P. Perdew, K. Burke, and M. Ernzerhof, "Generalized gradient approximation made simple," Phys. Rev. Lett. **77**, 3865–3868 (1996).
[89]J. P. Perdew, K. Burke, and M. Ernzerhof, "Generalized gradient approximation made simple [Phys. Rev. Lett. 77, 3865 (1996)]," Phys. Rev. Lett. **78**, 1396 (1997).
[90]A. P. Willard and D. Chandler, "Instantaneous liquid interfaces," J. Phys. Chem. B **114**, 1954–1958 (2010).
[91]F. Sedlmeier, D. Horinek, and R. R. Netz, "Nanoroughness, intrinsic density profile, and rigidity of the air-water interface," Phys. Rev. Lett. **103**, 136102 (2009).
[92]Z. G. Fthenakis, G. Kalosakas, G. D. Chatzidakis, C. Galiotis, K. Papagelis, and N. N. Lathiotakis, "Atomistic potential for graphene and other sp^2 carbon systems," Phys. Chem. Chem. Phys. **19**, 30925–30932 (2017).
[93]W. J. Hamer and Y. Wu, "Osmotic coefficients and mean activity coefficients of uni-univalent electrolytes in water at 25 °C," J. Phys. Chem. Ref. Data **1**, 1047–1100 (1972).
[94]C. Vega and E. de Miguel, "Surface tension of the most popular models of water by using the test-area simulation method," J. Chem. Phys. **126**, 154707 (2007).
[95]G. Luo, S. Malkova, J. Yoon, D. G. Schultz, B. Lin, M. Meron, I. Benjamin, P. Vanýsek, and M. L. Schlossman, "Ion distributions near a liquid-liquid interface," Science **311**, 216–218 (2006).
[96]D. Horinek and R. R. Netz, "Specific ion adsorption at hydrophobic solid surfaces," Phys. Rev. Lett. **99**, 226104 (2007).
[97]B. Hou, W. Bu, G. Luo, P. Vanýsek, and M. L. Schlossman, "Ion distributions at electrified water-organic interfaces: PB-PMF calculations and impedance spectroscopy measurements," J. Electrochem. Soc. **162**, H890 (2015).
[98]A. Schlaich, A. P. dos Santos, and R. R. Netz, "Simulations of nanoseparated charged surfaces reveal charge-induced water reorientation and nonadditivity of hydration and mean-field electrostatic repulsion," Langmuir **35**, 551–560 (2019).
[99]I. Borukhov, D. Andelman, and H. Orland, "Steric effects in electrolytes: A modified Poisson-Boltzmann equation," Phys. Rev. Lett. **79**, 435–438 (1997).
[100]A. A. Kornyshev, "Double-layer in ionic liquids: Paradigm change?," J. Phys. Chem. B **111**, 5545–5557 (2007).
[101]R. Liu, C. Zhang, X. Liang, J. Liu, X. Wu, and M. Chen, "Structural and dynamic properties of solvated hydroxide and hydronium ions in water from *ab initio* modeling," J. Chem. Phys. **157**, 024503 (2022).
[102]J. L. Fulton and M. Balasubramanian, "Structure of hydronium (H_3O^+)/chloride (Cl^-) contact ion pairs in aqueous hydrochloric acid solution: A Zundel-like local configuration," J. Am. Chem. Soc. **132**, 12597–12604 (2010).
[103]M. D. Baer, J. L. Fulton, M. Balasubramanian, G. K. Schenter, and C. J. Mundy, "Persistent ion pairing in aqueous hydrochloric acid," J. Phys. Chem. B **118**, 7211–7220 (2014).
[104]M. D. Baer, D. J. Tobias, and C. J. Mundy, "Investigation of interfacial and bulk dissociation of HBr, HCl, and HNO_3 using density functional theory-based molecular dynamics simulations," J. Phys. Chem. C **118**, 29412–29420 (2014).
[105]T. Ohto, H. Tada, and Y. Nagata, "Structure and dynamics of water at water–graphene and water–hexagonal boron-nitride sheet interfaces revealed by *ab initio* sum-frequency generation spectroscopy," Phys. Chem. Chem. Phys. **20**, 12979–12985 (2018).
[106]Y. Wang, F. Tang, X. Yu, T. Ohto, Y. Nagata, and M. Bonn, "Heterodyne-detected sum-frequency generation vibrational spectroscopy reveals aqueous molecular structure at the suspended graphene/water interface," Angew. Chem., Int. Ed. **63**, e202319503 (2024).
[107]P. Loche, L. Scalfi, M. Ali Amu, O. Schullian, D. J. Bonthuis, B. Rotenberg, and R. R. Netz, "Effects of surface rigidity and metallicity on dielectric properties and ion interactions at aqueous hydrophobic interfaces," J. Chem. Phys. **157**, 094707 (2022).
[108]L. Bennett, B. Melchers, and B. Proppe, "Curta: A general-purpose high-performance computer at ZEDAT, Freie Universität Berlin," 2020, http://dx.doi.org/10.17169/refubium-26754.